

# The CO-to-H<sub>2</sub> Conversion Factor of Galactic Giant Molecular Clouds using CO isotopologues: High-resolution $X_{\text{CO}}$ maps

Mikito Kohno<sup>1,2\*</sup>, and Yoshiaki Sofue<sup>3</sup>

<sup>1</sup>*Astronomy Section, Nagoya City Science Museum, 2-17-1 Sakae, Naka-ku, Nagoya, Aichi 460-0008, Japan*

<sup>2</sup>*Department of Physics, Graduate School of Science, Nagoya University, Furo-cho, Chikusa-ku, Nagoya, Aichi 464-8602, Japan*

<sup>3</sup>*Institute of Astronomy, The University of Tokyo, Mitaka, Tokyo 181-0015, Japan*

Accepted 2023 November 22. Received 2023 November 1; in original form 2023 May 9

## ABSTRACT

We investigated the correlation between intensities of the <sup>12</sup>CO and <sup>13</sup>CO ( $J = 1-0$ ) lines toward the Galactic giant molecular clouds (GMCs) W51A, W33, N35-N36 complex, W49A, M17SW, G12.02-00.03, W43, and M16 using the FUGIN (FOREST Unbiased Galactic plane Imaging survey with the Nobeyama 45-m telescope) CO line data. All the GMCs show intensity saturation in the <sup>12</sup>CO line when the brightness temperature of <sup>13</sup>CO is higher than a threshold temperature of about  $\sim 5$  K. We obtained high-resolution ( $\sim 20''$ ) distribution maps of the  $X_{\text{CO}}$  factor ( $X_{\text{CO,iso}}$ ) in individual GMCs using correlation diagrams of the CO isotopologues. It is shown that  $X_{\text{CO,iso}}$  is variable in each GMC within the range of  $X_{\text{CO,iso}} \sim (0.9-5) \times 10^{20} \text{ cm}^{-2} (\text{K km s}^{-1})^{-1}$ . Despite the variability in the GMCs, the average value among the GMCs is found to be nearly constant at  $X_{\text{CO,iso}} = (2.17 \pm 0.27) \times 10^{20} \text{ cm}^{-2} (\text{K km s}^{-1})^{-1}$ , which is consistent with that from previous studies in the Milky Way.

**Key words:** ISM: clouds – ISM: general – ISM: molecules – radio lines: ISM

## 1 INTRODUCTION

Giant molecular clouds (GMC) mainly consist of hydrogen molecules (H<sub>2</sub>) and are the sites of star formation in galaxies (Blitz et al. 2007; Fukui & Kawamura 2010; Dobbs et al. 2014; Chevance et al. 2023). The hydrogen molecule is difficult to observe directly because it has no an electric dipole moment for its homonuclear diatomic nature. Therefore, we often observe carbon monoxide (CO) with rotational transitions at millimeter wavelengths (Heyer & Dame 2015) and convert the intensity to the H<sub>2</sub> column density using the CO-to-H<sub>2</sub> conversion factor (hereafter  $X_{\text{CO}}$ ), which is given by

$$X_{\text{CO}} = N_{\text{H}_2} / W_{12\text{CO}} [\text{cm}^{-2} (\text{K km s}^{-1})^{-1}], \quad (1)$$

where  $W_{12\text{CO}}$  and  $N_{\text{H}_2}$  are the <sup>12</sup>CO  $J = 1-0$  integrated intensity and column density of hydrogen molecules, respectively (Bolatto et al. 2013).

The conversion factor has been obtained in various methods by comparing CO luminosity with virial mass (e.g., Solomon et al. 1987; Scoville et al. 1987), visual or infrared extinction (e.g., Frerking et al. 1982; Lombardi et al. 2006; Pineda et al. 2008; Lee et al. 2018), X-ray absorption (e.g., Sofue & Kataoka 2016), gamma-ray brightness (e.g., Strong et al. 1988; Abdo et al. 2010; Planck Collaboration et al. 2015; Hayashi et al. 2019b), and dust emission (e.g., Planck Collaboration et al. 2011; Leroy et al. 2011; Sandstrom et al. 2013; Fukui et al. 2014; Okamoto et al. 2017; Hayashi et al. 2019a; Yasuda et al. 2023). The values have been discussed in the Milky Way and Local Group galaxies, and their dependence on metallicity has been suggested (e.g., Wilson 1995; Arimoto et al. 1996; Sakamoto 1996; Dame et al. 2001; Mizuno et al. 2001; Rosolowsky et al. 2003; Fukui

& Kawamura 2010; Liszt et al. 2010; Leroy et al. 2011; Lee et al. 2014; Lin et al. 2016; Muraoka et al. 2017; Pitts & Barnes 2021; Ohno et al. 2023). The often used value currently in the Milky Way is  $X_{\text{CO}} = 2.0 \times 10^{20} \text{ cm}^{-2} (\text{K km s}^{-1})^{-1}$ , having an uncertainty of  $\pm 30\%$  (Bolatto et al. 2013).

Recently, Sofue & Kohno (2020) (hereafter paper I) proposed a new method to estimate the molecular cloud mass considering the variability of the  $X_{\text{CO}}$  factor from the correlation between <sup>12</sup>CO and <sup>13</sup>CO. Paper I analyzed only two Galactic GMCs of M16 (Sofue 2020b; Nishimura et al. 2021) and W43 (Sofue et al. 2019; Sofue 2021; Kohno et al. 2021), while the spatial distributions of  $X_{\text{CO}}$  inside the GMCs have not yet been discussed.

In this paper, we extend the analysis of Paper I, aiming to reveal the variability of  $X_{\text{CO}}$  within the molecular cloud of scales ( $\sim 10-50$  pc) at sub-pc resolutions ( $\sim 20''$ ). The target GMCs are W51A (Fujita et al. 2021), W33 (Kohno et al. 2018; Murase et al. 2022), W49A (Miyawaki et al. 2022), N35-N36 complex (Torii et al. 2018; Sofue 2019a,b), M17SW (Nishimura et al. 2018; Sofue 2020a, 2022), G012.02-00.03 (Sanna et al. 2014), W43 (Sofue et al. 2019; Kohno et al. 2021), and M16 (Sofue 2020b; Nishimura et al. 2021). These GMCs are also known as massive star-forming regions in the Milky Way. The basic parameters of these GMCs are summarized in Table 1.

This paper is structured as follows: section 2 introduces the FUGIN (FOREST Unbiased Galactic plane Imaging survey with the Nobeyama 45-m telescope) data; section 3 presents the methods of analysis; in section 4, we demonstrate the results; in section 5, we discuss the variability of the  $X_{\text{CO}}$  factor, and in section 6, we summarize the results.

\* E-mail: mikito.kohno@gmail.com, kohno@nagoya-p.jp

**Table 1.** Properties of the Galactic massive star forming regions

Name	$l$ [deg]	$b$ [deg]	$V_{\text{LSR}}$ [km s $^{-1}$ ]	$D$ [kpc]	$R_{\text{G}}$ [kpc]	$T_{\text{rms}} (^{13}\text{CO } J=1-0)$ [K]	$T_{\text{rms}} (^{12}\text{CO } J=3-2)$ [K]	Reference
(1)	(2)	(3)	(4)	(5)	(6)	(7)	(8)	(9)
W51A	49.5	-0.4	57	5.4	6.1	~ 0.6	~ 0.9	[1]
W33	12.8	-0.2	35	2.4	5.7	~ 0.6	~ 0.4	[2]
N35-N36 complex	24.5	0.1	110	7.3	3.3	~ 0.6	~ 0.5	[3,4]
W49A	43.16	0.0	11	11	7.5	~ 0.5	~ 0.4	[5]
M17SW	15.0	-0.7	20	2.0	6.1	~ 0.7	—	[6,7,8]
G012.02-00.03	12.02	-0.03	112	9.4	2.3	~ 0.7	~ 0.3	[9]
W43	30.8	0.0	95	5.5	4.3	~ 0.9	~ 0.4	[10,11]
M16	17.1	0.7	23	2.0	6.1	~ 0.7	—	[12,13]

Columns: (1) Name. (2) Galactic longitude (3) Galactic latitude (4) Radial velocity (5) Distance from the solar system (6) Distance from the Galactic center. The distance to the Galactic centre from the solar system is assumed to be  $R_0 = 8.0$  kpc obtained by the mean value of the very long baseline interferometry (VLBI) astrometry results (VERA Collaboration et al. 2020; Reid et al. 2019). (7) r.m.s noise levels of the  $^{13}\text{CO } J=1-0$  data (8) r.m.s noise levels of the  $^{12}\text{CO } J=3-2$  data (9) References [1] Fujita et al. (2021) [2] Kohno et al. (2018) [3] Torii et al. (2018) [4] Sofue (2019a) [5] Miyawaki et al. (2022) [6] Nishimura et al. (2018) [7] Sofue (2020a) [8] Yamagishi et al. (2016) [9] Sanna et al. (2014) [10] Sofue et al. (2019) [11] Kohno et al. (2021) [12] Sofue (2020b) [13] Nishimura et al. (2021)

## 2 DATA

We utilized the  $^{12}\text{CO}$  and  $^{13}\text{CO } J=1-0$  line data obtained with the Nobeyama 45 m telescope (FUGIN: Umemoto et al. 2017; Torii et al. 2019; Fujita et al. 2023). The rest frequencies of  $^{12}\text{CO}$  and  $^{13}\text{CO } J=1-0$  are 115.271 GHz and 110.201 GHz, respectively. The front end was the FOUr beam REceiver System on the 45-m Telescope (FOREST: Minamidani et al. 2016; Nakajima et al. 2019), which is the four-beam, side-band separating (2SB), and dual-polarization superconductor-insulator-superconductor (SIS) receiver. The observations were performed in the on-the-fly mapping mode (Sawada et al. 2008). The back-end system was used an FX-type spectrometer named SAM 45 (Kuno et al. 2011; Kamazaki et al. 2012). The half-power beam width (HPBW) of the 45 m telescope is  $14''$  and  $15''$  at 115 GHz and 110 GHz, respectively. The data are gridded to  $8.5''$  and  $0.65 \text{ km s}^{-1}$  for the spatial and velocity space. The final 3D cube used in this study has a voxel size of  $(l, b, v) = (8.5'', 8.5'', 0.65 \text{ km s}^{-1})$ . The effective resolution convolved with a Bessel  $\times$  Gaussian function is  $20''$  and  $21''$  for  $^{12}\text{CO}$  and  $^{13}\text{CO } J=1-0$ , respectively. We subtracted the baselines using a first-order polynomial function from each spectrum. The baseline ranges are adopted from  $-200 \text{ km s}^{-1}$  to  $-50 \text{ km s}^{-1}$  and  $200 \text{ km s}^{-1}$  to  $350 \text{ km s}^{-1}$  for the first Galactic quadrant with the FUGIN CO survey (Umemoto et al. 2017). The data are calibrated from the antenna temperature ( $T_A^*$ ) to the main-beam temperature ( $T_{\text{MB}}$ ) by measuring the main-beam efficiency of 0.43 for  $^{12}\text{CO}$ , 0.45 for  $^{13}\text{CO}$ , and  $\text{C}^{18}\text{O}$  using standard calibration sources. Detailed information on the FUGIN project is summarized in the project overview paper by Umemoto et al. (2017). Cube data calibrated to the main-beam temperature are available at the Japanese Virtual Observatory (JVO). We also used the  $^{12}\text{CO } (J=3-2)$  High-Resolution Survey (COHRS) archival data of the Galactic Plane obtained by the James Clark Maxwell Telescope (Dempsey et al. 2013; Park et al. 2023). The cube data are converted  $T_A^*$  to the  $T_{\text{MB}}$  scale using a main-beam efficiency of 0.61 (Park et al. 2023). The spatial and velocity resolutions are  $16.6''$  and  $0.635 \text{ km s}^{-1}$ , respectively. Comparing the FUGIN CO survey data, we smoothed them to  $20''$  with the same spatial resolution. The  $^{12}\text{CO } J=3-2$  data are re-gridded to the same voxel size as the FUGIN data using CASA (CASA Team et al. 2022). Table 1 presents the root-mean-square noise level of each GMC at the  $T_{\text{MB}}$  scale.

## 3 METHODS

We derived the  $\text{H}_2$  column density per velocity channel using the local thermal equilibrium (LTE) method and the  $X_{\text{CO}}$  factor, as described in Paper I and Pineda et al. (2008). The brightness temperature ( $T_{\text{B}}$ ) of the CO line intensity with the excitation temperature ( $T_{\text{ex}}$ ) and optical depth ( $\tau$ ) is given by

$$T_{\text{B}} = T_0 \left( \frac{1}{e^{T_0/T_{\text{ex}}} - 1} - \frac{1}{e^{T_0/T_{\text{bg}}} - 1} \right) (1 - e^{-\tau}) \text{ [K]}, \quad (2)$$

where  $T_{\text{bg}} = 2.725 \text{ K}$  is the temperature of the cosmic microwave background radiation.  $T_0 = h\nu/k$  is the Planck temperature with  $h$ ,  $\nu$ , and  $k$  being the Planck constant, rest frequency, and Boltzmann constant, respectively. If we assume that the  $^{12}\text{CO}$  line is optically thick, the excitation temperature is given by

$$T_{\text{ex}} = T_0^{115} \left/ \ln \left( 1 + \frac{T_0^{115}}{T_{\text{B}}(^{12}\text{CO})_{\text{max}} + 0.83632} \right) \right. \text{ [K]}, \quad (3)$$

where  $T_{\text{B}}(^{12}\text{CO})_{\text{max}}$  and  $T_0^{115} = 5.53194$  correspond to the  $^{12}\text{CO}$  peak intensity and the Planck temperature at the rest frequency of  $^{12}\text{CO } J=1-0$ , respectively. We assume that  $T_{\text{ex}}$  is equal in the  $^{12}\text{CO}$  and  $^{13}\text{CO}$  line emissions, and express the optical depth as follows:

$$\tau(^{13}\text{CO}) = -\ln \left( 1 - \frac{T_{\text{B}}(^{13}\text{CO})_{\text{max}}/T_0^{110}}{(e^{T_0^{110}/T_{\text{ex}}} - 1)^{-1} - 0.167667} \right), \quad (4)$$

where  $T_{\text{B}}(^{13}\text{CO})_{\text{max}}$  and  $T_0^{110} = 5.28864$  represent the  $^{13}\text{CO}$  peak intensity and the Planck temperature at the rest frequency of  $^{13}\text{CO } J=1-0$ , respectively (Pineda et al. 2008). According to Wilson et al. (2009), the  $^{13}\text{CO}$  column density is given by

$$N_{^{13}\text{CO}} = 3.0 \times 10^{14} \frac{\tau}{1 - e^{-\tau}} \frac{1}{1 - e^{-T_0^{110}/T_{\text{ex}}}} I_{^{13}\text{CO}} \text{ [cm}^{-2}\text{]}, \quad (5)$$

where  $I_{^{13}\text{CO}}$  is the  $^{13}\text{CO}$  integrated intensity. Then, we converted  $N_{^{13}\text{CO}}$  to the  $\text{H}_2$  column density using the abundance ratio of  $\text{H}_2$  to  $^{13}\text{CO}$  molecules given by

$$N_{\text{H}_2}(^{13}\text{CO}) = Y_{^{13}\text{CO}} N_{^{13}\text{CO}} \text{ [cm}^{-2}\text{]}. \quad (6)$$

Here,  $Y_{^{13}\text{CO}}$  is adopted as  $(5.0 \pm 2.5) \times 10^5$  (Dickman 1978) following Paper I.

We then calculated the  $\text{H}_2$  column density per velocity channel,



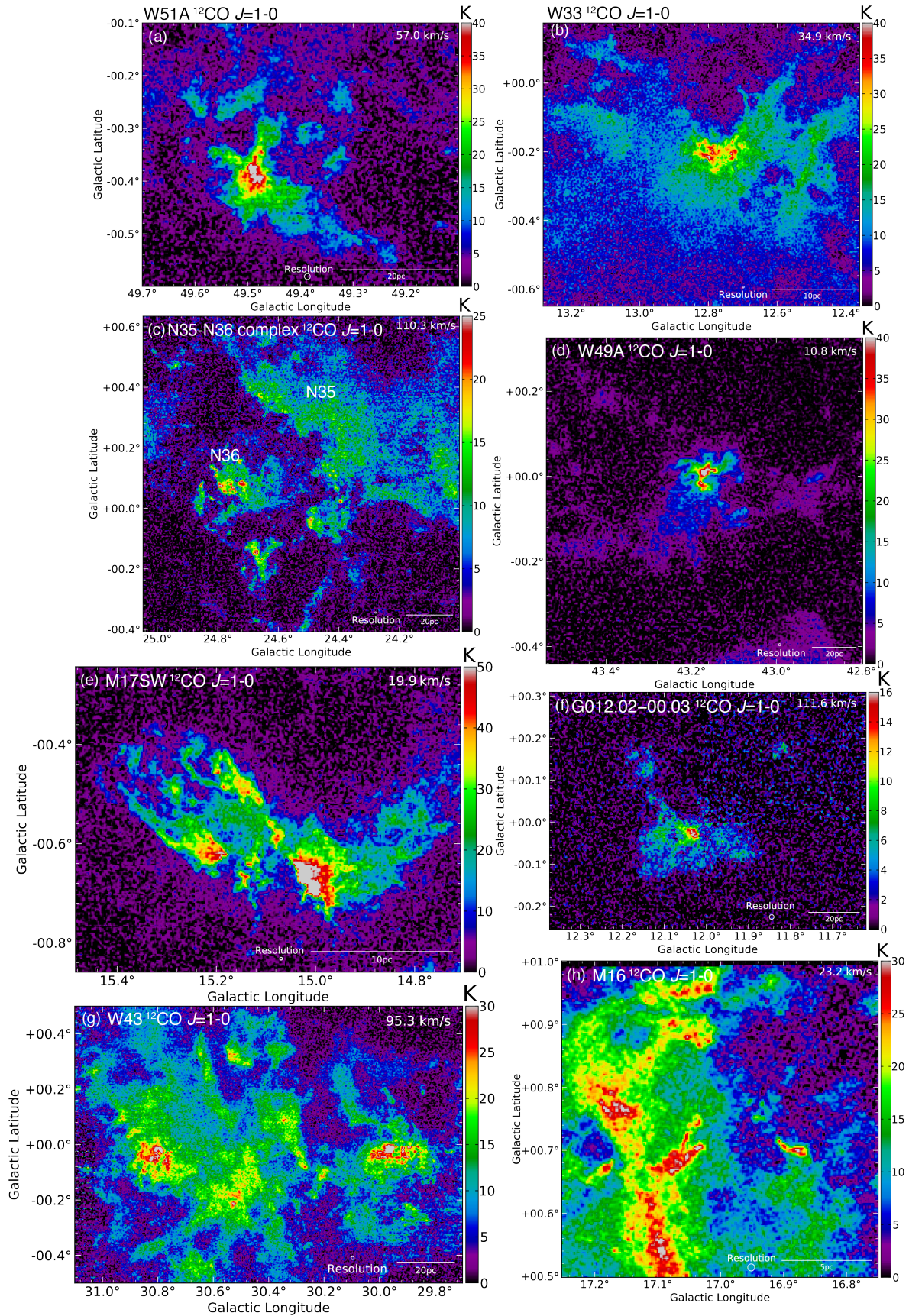


**Figure 1.** The  $^{12}\text{CO}$  peak intensity maps of (a) W51A at the radial velocity of  $57.0 \text{ km s}^{-1}$ , (b) W33 at  $34.9 \text{ km s}^{-1}$ , (c) N35-N36 complex at  $110.3 \text{ km s}^{-1}$ , (d) W49A at  $10.8 \text{ km s}^{-1}$ , (e) M17SW at  $19.9 \text{ km s}^{-1}$ , (f) G012.02-00.03 at  $111.6 \text{ km s}^{-1}$ , (g) W43 at  $95.3 \text{ km s}^{-1}$ , and (h) M16 at  $23.2 \text{ km s}^{-1}$ .

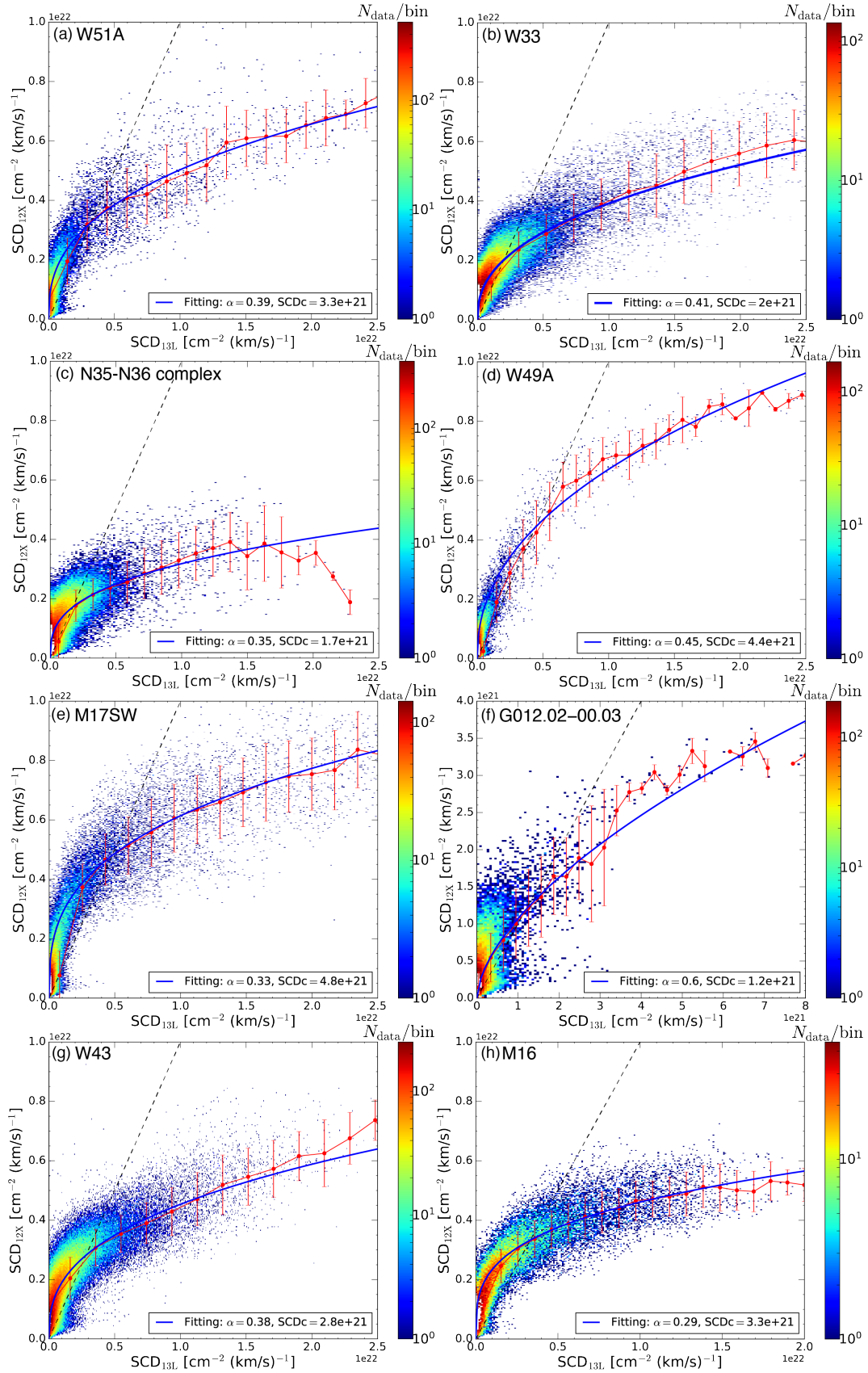


**Figure 2.** Scatter plots between  $SCD_{13L}$  and  $SCD_{12X}$  of (a) W51A, (b) W33, (c) the N35-N36 complex, (d) W49A, (e) M17SW, (f) G012.02-00.03, (g) W43, and (h) M16. Red points show the averaged values of each bin, and the error bars are standard deviations of  $SCD_{12X}$ . Blue curves indicate the fitting results of scatter plots. The black dashed lines indicate the linear relation of  $SCD_{12X} = SCD_{13L}$ . The color bars show the number of data points in a bin. ( $N_{\text{data}}/\text{bin}$ )



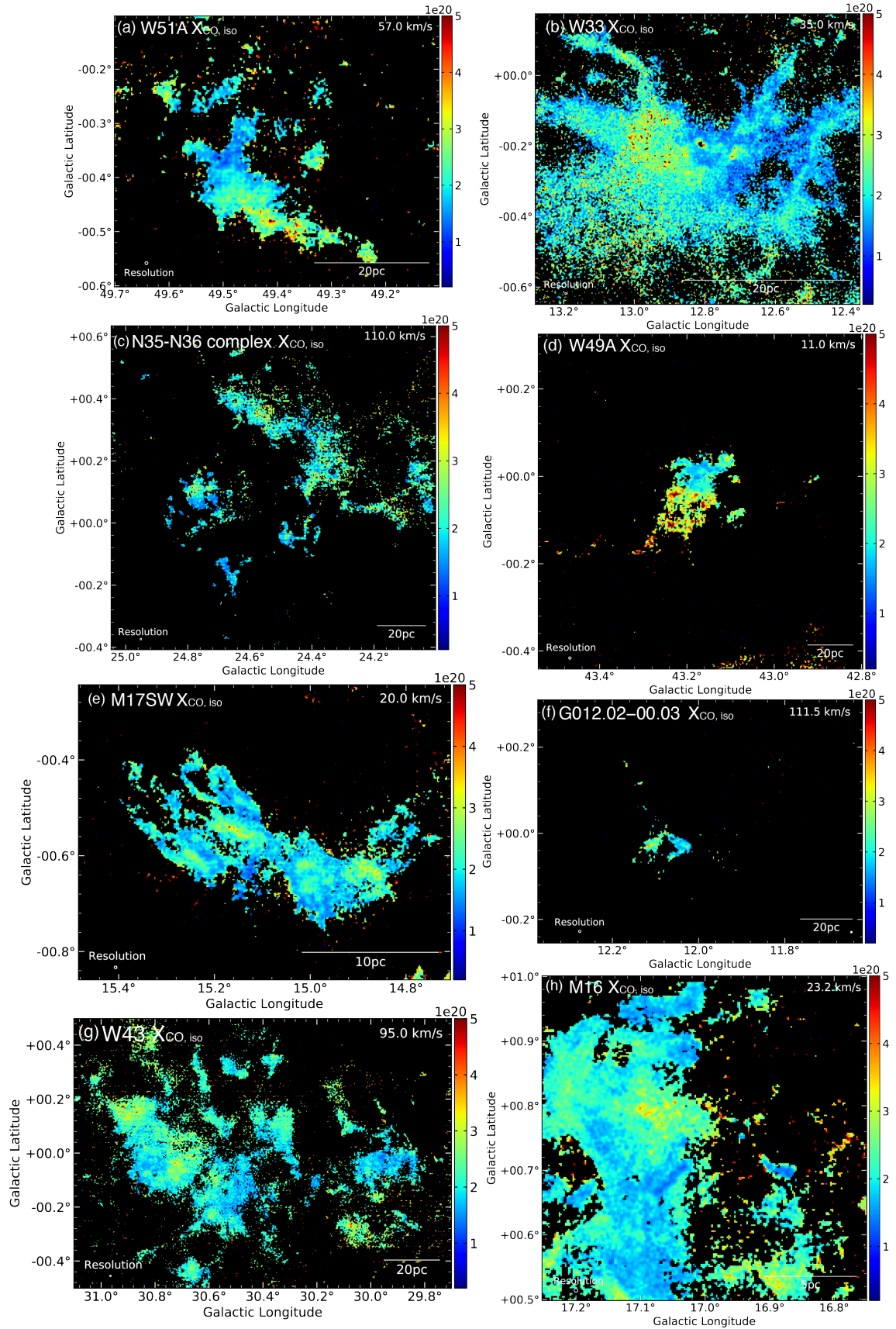


**Figure 3.** Spatial distributions of  $X_{\text{CO,iso}}$  in (a) W51A, (b) W33, (c) the N35-N36 complex, (d) W49A, (e) M17SW, (f) G012.02-00.03, (g) W43, and (h) M16. The points are plotted of  $T_{\text{B}}(^{13}\text{CO}) > 3\sigma$ . The  $1\sigma$  noise level of each GMC is presented in Table 1.

which is defined as the spectral column density, using the  $X_{\text{CO}}$  and LTE method from the intensity of  $^{12}\text{CO}$  and  $^{13}\text{CO}$ , as described in Paper I. The spectral column densities (SCD) of  $^{12}\text{CO}$  and  $^{13}\text{CO}$  are expressed as

$$\text{SCD}_{12\text{X}} = \frac{dN_{\text{H}_2}(^{12}\text{CO})}{dv} = X_{\text{CO}} T_{\text{B}}(^{12}\text{CO}) [\text{cm}^{-2}(\text{km s}^{-1})^{-1}], \quad (7)$$

and

$$\begin{aligned} \text{SCD}_{13\text{L}} &= \frac{dN_{\text{H}_2}(^{13}\text{CO})}{dv} \\ &= 3.0 \times 10^{14} \frac{\tau}{1 - e^{-\tau}} \frac{Y_{13\text{CO}} T_{\text{B}}(^{13}\text{CO})}{1 - e^{-T_0^{10}/T_{\text{ex}}}} [\text{cm}^{-2}(\text{km s}^{-1})^{-1}]. \end{aligned} \quad (8)$$

Here,  $\text{SCD}_{12\text{X}}$  and  $\text{SCD}_{13\text{L}}$  are the  $\text{H}_2$  column densities at the peak velocity channels, assuming a standard (normalization) value of  $X_{\text{CO}} = 2.0 \times 10^{20} \text{ cm}^{-2} (\text{K km s}^{-1})^{-1}$  (Bolatto et al. 2013) and  $Y_{13\text{CO}} = 5.0 \times 10^5$  (Dickman 1978), respectively.

## 4 RESULTS

### 4.1 Correlation between $\text{SCD}_{12\text{X}}$ and $\text{SCD}_{13\text{L}}$

Figure 1(a-h) shows the  $^{12}\text{CO } J=1-0$  peak intensity maps of W51A, W33, N35-N36 complex, W49A, M17SW, G012.02-00.03, W43, and M16 GMC. W49A and G012.02-00.03 GMC show compact CO distributions of  $\sim 20$  pc, while W33, N35-N36 complex, W43, and M16 have more diffuse distributions of molecular gas with about the half-intensity level of the peak brightness temperature.

Figure 2(a-h) presents scatter plots between  $\text{SCD}_{12\text{X}}$  and  $\text{SCD}_{13\text{L}}$  of GMCs presented in Figure 1(a-h). Black dashed lines show the linear relation of  $\text{SCD}_{12\text{X}} = \text{SCD}_{13\text{L}}$ .  $\text{SCD}_{12\text{X}}$  shows saturation at high  $\text{SCD}_{13\text{L}}$ , and the nonlinear relation of each GMC has different saturation levels. Indeed, previous studies have reported that the  $^{12}\text{CO}$  intensity shows apparent saturation at the high-intensity level of  $^{13}\text{CO}$  from the observation of Galactic molecular clouds (Langer et al. 1989; Pineda et al. 2008; Yoda et al. 2010). Curve fitting is useful for quantitatively evaluating the nonlinear relationship between the  $^{12}\text{CO}$  and  $^{13}\text{CO}$  intensities. Here, we performed curve fitting to the scatter plots between  $\text{SCD}_{12\text{X}}$  and  $\text{SCD}_{13\text{L}}$  using the free parameters of  $\alpha$  and  $\text{SCD}_{\text{c}}$  (spectral column density coefficient), as in Paper I.  $\text{SCD}_{12\text{X}}$  is given by

$$\text{SCD}_{12\text{X}} = \text{SCD}_{\text{c}} \left( \frac{\text{SCD}_{13\text{L}}}{\text{SCD}_{\text{c}}} \right)^{\alpha}. \quad (9)$$

Blue curves show the fitting results for individual GMCs. To confirm whether the scatter plots shown in Figure 2 depend on the physical resolutions due to different distances from the GMCs, we smoothed the data of GMCs to the same physical resolution and grid size of  $\sim 1$  pc and  $\sim 0.45$  pc. This physical resolution corresponds to a beam size of  $\sim 20''$  at the distance of W49A, the GMC furthest from us in this study. In Figures A1 and A2(a-h) of the Appendix, we show the obtained peak intensity maps and scatter plots of GMCs for equal physical resolution. The results are almost the same as those in Figure 2. The fitting parameters have the range of  $\alpha = 0.30-0.54$  and  $\text{SCD}_{\text{c}} = (1.6-4.4) \times 10^{21} \text{ cm}^{-2} (\text{km s}^{-1})^{-1}$ . Thus, we find that the opacity and internal clump sizes in a GMC do not affect the relation of the  $^{12}\text{CO}$  and  $^{13}\text{CO}$  correlation. Our analysis also shows that the saturation level of correlations does not depend on physical spatial resolution and pixel size.

### 4.2 Spatial distributions of $X_{\text{CO,iso}}$ in the Galactic GMCs

We obtained the  $X_{\text{CO}}$  factor (hereafter  $X_{\text{CO,iso}}$ ) of each GMC from the correlation between  $\text{SCD}_{12\text{X}}$  and  $\text{SCD}_{13\text{L}}$ .  $X_{\text{CO,iso}}$  at each pixel of the molecular clouds is expressed as follows:

$$X_{\text{CO,iso}} = \text{SCD}_{\text{c}} \left( \frac{\text{SCD}_{13\text{L}}}{\text{SCD}_{\text{c}}} \right)^{\alpha} / T_{\text{B}}(^{12}\text{CO}) [\text{cm}^{-2}(\text{K km s}^{-1})^{-1}], \quad (10)$$

where  $\alpha$  and  $\text{SCD}_{\text{c}}$  are the fitting parameters obtained in Figures 2 and A2.

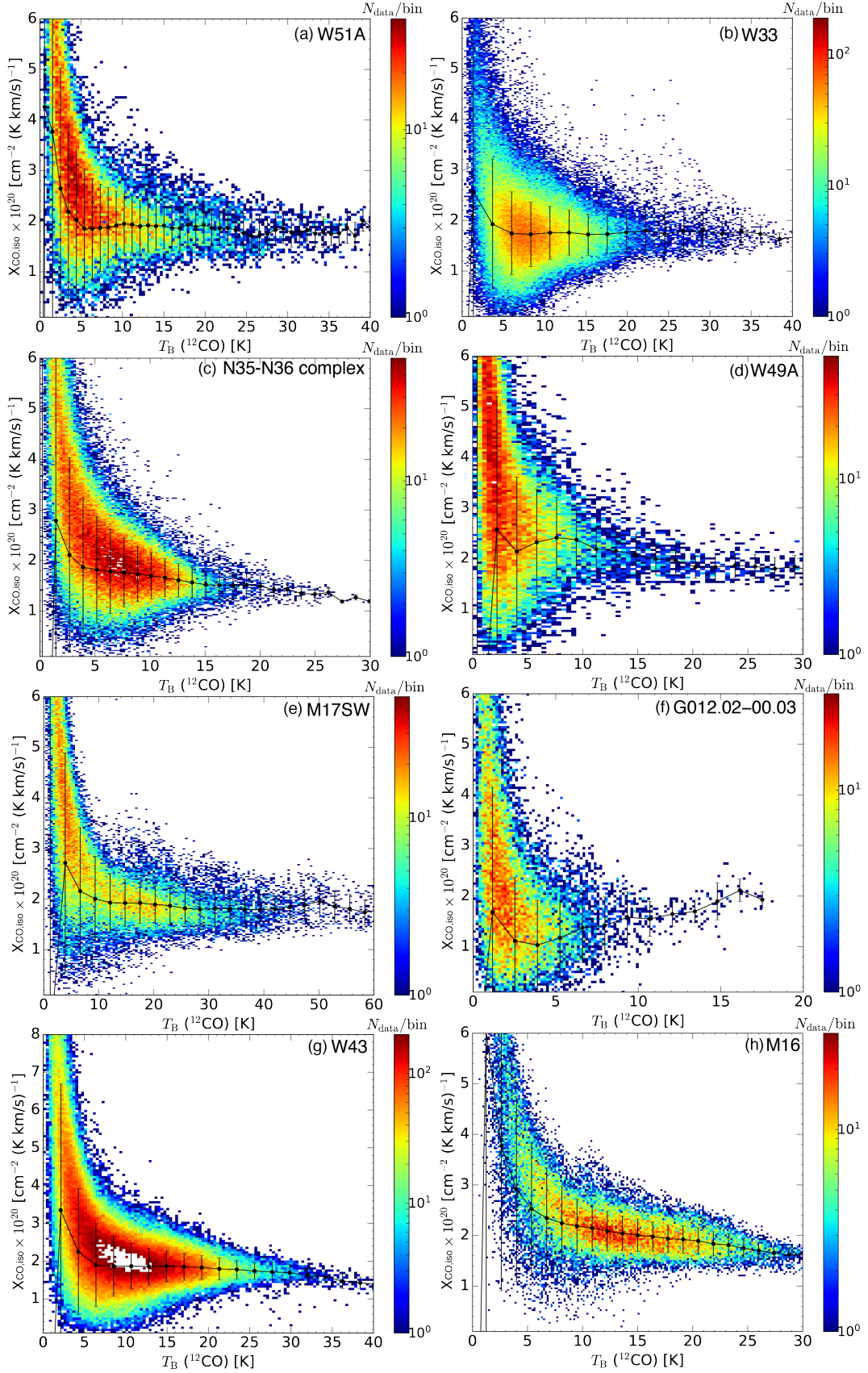
Figure 3(a-h) shows the  $X_{\text{CO,iso}}$  maps of each GMC.  $X_{\text{CO,iso}}$  has a variability with the range of  $(0.9-5.0) \times 10^{20} [\text{cm}^{-2}(\text{K km s}^{-1})^{-1}]$  in a GMC. Comparing Figure 1 and Figure 3, we find an anti-correlation between the  $^{12}\text{CO}$  peak intensity and  $X_{\text{CO,iso}}$ . Figure 4 shows the scatter plot between  $X_{\text{CO,iso}}$  and  $T_{\text{B}}(^{12}\text{CO})$  in each GMC.  $X_{\text{CO,iso}}$  monotonically decreases with increasing brightness temperature, except for G012.02-00.03. It also shows a lower limit around  $X_{\text{CO}} \sim 2 \times 10^{20} \text{ cm}^{-2} (\text{K km s}^{-1})^{-1}$  above  $T(^{12}\text{CO}) > 20$  K. These results may correspond to the saturation of the  $^{12}\text{CO}$  intensity in the dense cores of the GMC. This is consistent with previous studies of Perseus molecular clouds obtained by the correlation between the  $^{12}\text{CO}$  integrated intensity and  $\text{H}_1$  column number density derived from the optical depth of 353 GHz dust emission ( $\tau_{353}$ ) by Planck satellite observations (see Figure 12 and 15 in Okamoto et al. 2017).

Table 2 lists the results of parameter fitting for  $\alpha$ ,  $\text{SCD}_{\text{c}}$ ,  $X_{\text{CO,iso}}$ , and the correlation coefficient obtained from the resolution of Figure A2. The mean value of  $X_{\text{CO,iso}}$  of all GMCs in this study is  $(2.17 \pm 0.27) \times 10^{20} \text{ cm}^{-2} (\text{K km s}^{-1})^{-1}$ .  $X_{\text{CO,iso}}$  shows the local variability in the Galactic GMCs (Figure 3), while the mean value is consistent within the margin of error in previous works of  $2 \times 10^{20} \text{ cm}^{-2} (\text{K km s}^{-1})^{-1}$  (Bolatto et al. 2013),  $(1.8 \pm 0.3) \times 10^{20} \text{ cm}^{-2} (\text{K km s}^{-1})^{-1}$  (Dame et al. 2001), and  $(2.54 \pm 0.13) \times 10^{20} \text{ cm}^{-2} (\text{K km s}^{-1})^{-1}$  (Planck Collaboration et al. 2011).

## 5 DISCUSSION

### 5.1 The variability of $X_{\text{CO,iso}}$

Our fitting results show that the correlation of column densities between  $^{12}\text{CO}$  and  $^{13}\text{CO}$  is not universal in Galactic GMCs. Each GMC has its own correlation parameters (Figures 2 and A2). Weiß et al. (2001) reported that the  $X_{\text{CO}}$  factor for a virialized GMC depends on the kinetic temperature ( $T_{\text{kin}}$ ) and molecular hydrogen number density ( $n(\text{H}_2)$ ) of the molecular gas. (see also Chapter 2.1 in Bolatto et al. 2013). To reveal the origin of the variations in  $X_{\text{CO,iso}}$ , we investigated the  $^{12}\text{CO } J=3-2/1-0$  intensity ratio (hereafter  $R_{3-2/1-0}^{12}$ ) using the JCMT  $^{12}\text{CO } J=3-2$  archival data (Dempsey et al. 2013; Park et al. 2023).  $R_{3-2/1-0}^{12}$  depends on  $T_{\text{kin}}$  and  $n(\text{H}_2)$  in molecular clouds assuming the large velocity gradient model (Goldreich & Kwan 1974). We analyzed the W51, W33, N35, W49A, G12.02-00.03, and W43 GMC because the JCMT data are only covered with  $|b| < 0.5^\circ$ . Figure 5 shows the scatter plot between  $X_{\text{CO,iso}}$  and  $R_{3-2/1-0}^{12}$ . The plots of each GMC do not show a clear correlation. Thus, we suggest that the origin of own correlation parameters and variations of  $X_{\text{CO,iso}}$  might not be simply density and/or temperature variations in a molecular cloud. In our analysis, we assumed that  $Y_{13\text{CO}}$  is constant in all GMCs. We point out that the change of the isotope abundance ratio with density might explain the variability of  $X_{\text{CO,iso}}$  in a GMC.



**Figure 4.** Scatter plots between  $X_{\text{CO,iso}}$  and  $T_{\text{B}} (^{12}\text{CO})$  in (a) W51A, (b) W33, (c) the N35-N36 complex, (d) W49A, (e) M17SW, (f) G012.02-00.03, (g) W43, and (h) M16. Black points show the averaged values of each bin, and the error bars are standard deviations of  $X_{\text{CO,iso}}$ . The color bars show the number of data points in a bin. ( $N_{\text{data}}/\text{bin}$ )

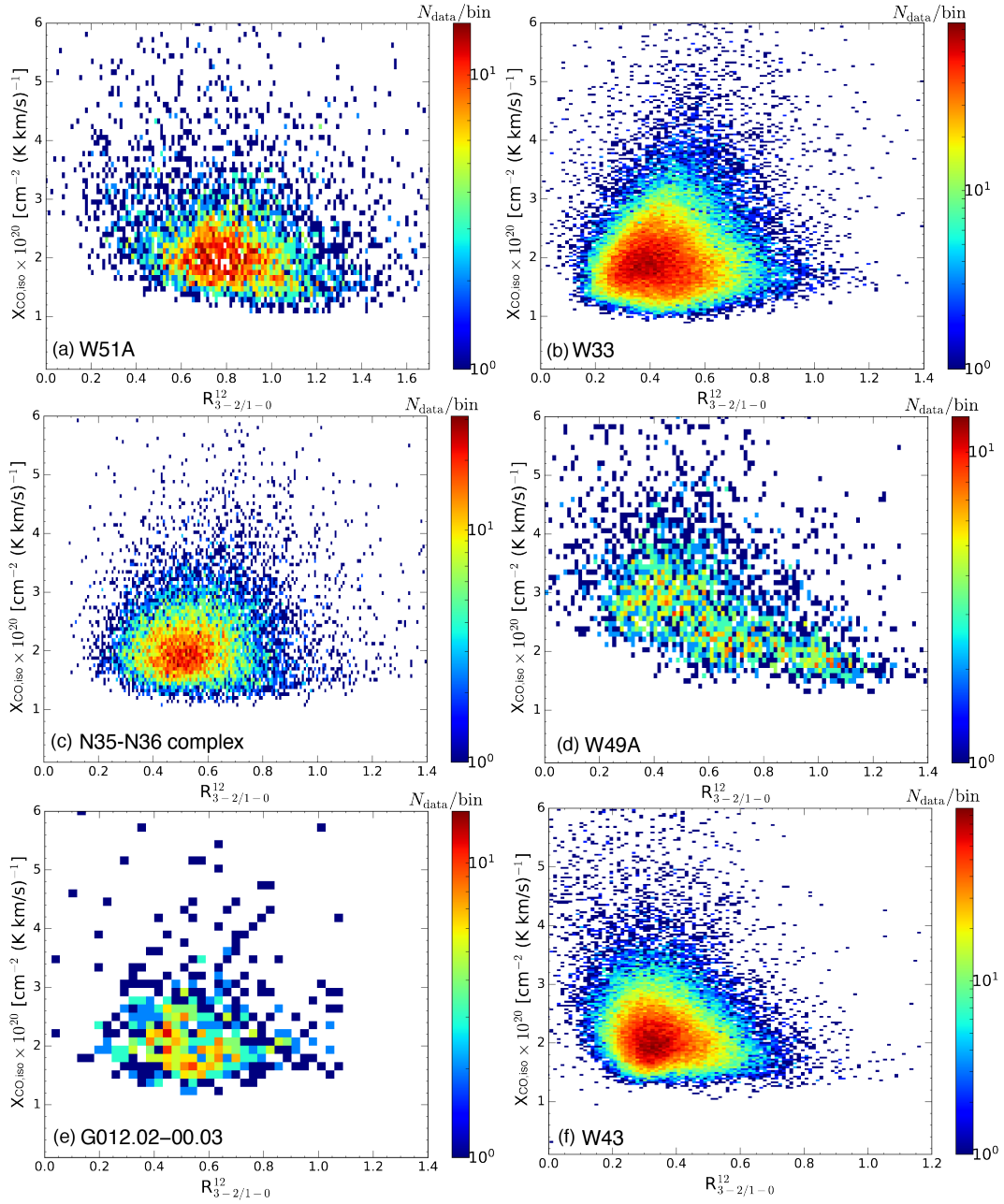


**Figure 5.** Scatter plots between  $X_{\text{CO,iso}}$  and  $R_{3-2/1-0}^{12}$  of (a) W51A, (b) W33, (c) the N35-N36 complex, (d) W49A, (e) G012.02-00.03, and (f) W43. The points are plotted of  $T_{\text{B}}(^{13}\text{CO}) > 3\sigma$ . The color bars show the number of data points in a bin. ( $N_{\text{data}}/\text{bin}$ )

## 5.2 Radial gradient of the $X_{\text{CO}}$ factor

In addition, we investigated the radial gradient of the  $X_{\text{CO}}$  factor in the Galactic disc. The averaged  $X_{\text{CO}}$  factor has a high value in W49A at Galactocentric distance  $R = 7.5$  kpc, while G012.02-00.03 has a low value  $R = 2.3$  kpc. According to [Arimoto et al. \(1996\)](#), the  $X_{\text{CO}}$  factor increases with the Galactocentric radius by an exponential function given by

$$\log_{10}\left(\frac{X_{\text{CO}}}{X_0}\right) = 0.41\frac{(R - R_0)}{r_e}, \quad (11)$$

where  $r_e = 6.2$  kpc is the scale radius of the Galactic disc and  $X_0$  is  $X_{\text{CO}}$  at  $R = R_0 = 8.0$  kpc ([VERA Collaboration et al. 2020](#); [Reid et](#)

[al. 2019](#)). This equation can be deformed as follows:

$$X_{\text{CO}} = 0.59 \times 10^{20} \exp\left(\frac{R}{6.567 [\text{kpc}]}\right) [\text{cm}^{-2}(\text{K km s}^{-1})^{-1}] \quad (12)$$

Figure 6 shows a plot of  $X_{\text{CO,iso}}$  obtained in this paper as a function of the Galactocentric distance. It is found that  $X_{\text{CO,iso}}$  increases with the distance from the Galactic Centre, and the plot may be fitted by an exponential function by

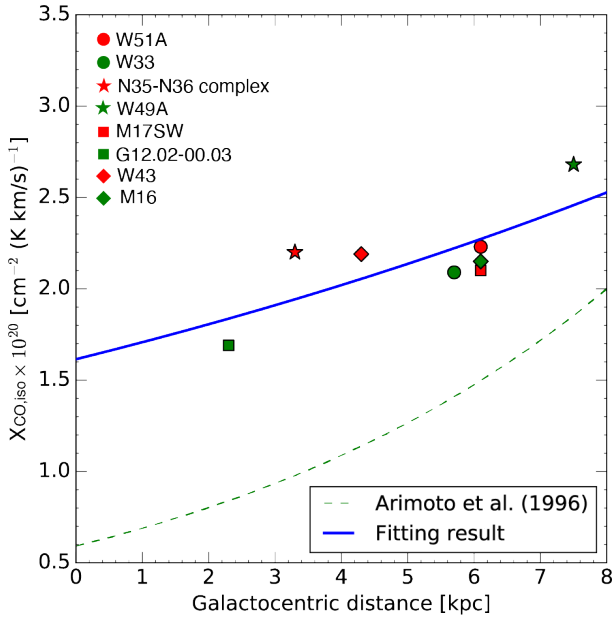
$$X_{\text{CO,iso}} = 1.61 \times 10^{20} \exp\left(\frac{R}{17.85[\text{kpc}]}\right) [\text{cm}^{-2}(\text{K km s}^{-1})^{-1}]. \quad (13)$$

Previous studies reported that a value of the  $X_{\text{CO}}$  factor depends on



**Table 2.** Fitting results and  $\langle X_{\text{CO,iso}} \rangle$  taken from the correlation of  $\text{SCD}_{12\text{X}}$  and  $\text{SCD}_{13\text{L}}$ .

Name	$\alpha$	$\text{SCD}_{\text{C}}$ [ $\times 10^{21} \text{ cm}^{-2} (\text{km s}^{-1})^{-1}$ ]	$\langle X_{\text{CO,iso}} \rangle$ [ $\times 10^{20} \text{ cm}^{-2} (\text{K km s}^{-1})^{-1}$ ]	C.C
(1)	(2)	(3)	(4)	(5)
W51A	0.39	3.3	2.23	0.76
W33	0.46	1.9	2.09	0.82
N35-N36	0.34	1.8	2.20	0.79
W49A	0.45	4.4	2.68	0.78
M17 SW	0.36	4.4	2.10	0.77
G012.02-00.03	0.54	1.6	1.69	0.69
W43	0.36	3.0	2.19	0.82
M16	0.30	3.3	2.15	0.89
Average	$0.40 \pm 0.08$	$2.96 \pm 1.11$	$2.17 \pm 0.27$	$0.79 \pm 0.06$

 Columns: (1) GMC names (2) The fitting parameter of the non-linear relation. (3) The coefficient of the spectrum column density ( $\text{SCD}_{\text{C}}$ ). (4) The mean value of  $X_{\text{CO,iso}}$  in a GMC. (5) Correlation coefficient. The errors of averaged value are adopted as the standard variation in all GMCs.

**Figure 6.** The  $X_{\text{CO,iso}}$  gradient from the distance of the Galactic Center. The blue line shows the fitting result adopted by the exponential function. The green dashed line indicates the relation from Arimoto et al. (1996).

the metal abundance in galaxies (e.g., Arimoto et al. 1996; Israel 1997; Leroy et al. 2011; Genzel et al. 2012). We suggest that the galactocentric dependency of  $X_{\text{CO,iso}}$  is caused by the radial metallicity gradient from the Galactic center to the outer Galaxy in the Milky Way. Our fitting result yields a significantly larger  $X_{\text{CO}}$  at the Galactic Centre by a factor of 3 compared to that by Arimoto et al. (1996) indicated by the green dashed line. This discrepancy may be caused by no data point within  $R < 2$  kpc in our study as well as by the normalization of the local value to  $2 \times 10^{20} [\text{H}_2 \text{ cm}^{-2} (\text{K km s}^{-1})^{-1}]$  at 8 kpc in the previous study. Sodroski et al. (1995) reported that the  $X_{\text{CO}}$  factor within 400 pc in the Galactic Centre region is by a factor 3-10 lower than the Galactic disk. Therefore, the value of  $X_{\text{CO}}$  in the Galactic Centre is still controversial. The present method applied to the  $^{12}\text{CO}$  and  $^{13}\text{CO}$   $J=1-0$  line data in the Galactic Centre region would provide a more precise determination of  $X_{\text{CO}}$  in the

innermost Milky Way. A detailed analysis of this point will be presented in a separate paper using the CO survey data of the Galactic Centre (e.g., Oka et al. 1998; Torii et al. 2010; Enokiya et al. 2014; Tokuyama et al. 2019).

### 5.3 Comparison with the virial methods

Finally, we calculated the  $X_{\text{CO}}$  factor from the virial mass of each GMC compared with our estimation. According to Solomon et al. (1987), the virial mass of GMCs is given by

$$M_{\text{vir}} = 1040 R \sigma_v^2 [M_{\odot}], \quad (14)$$

where  $R$  is the effective radius of a GMC in parsec and  $\sigma_v$  is the 1D velocity dispersion in  $\text{km s}^{-1}$ , assuming a density profile of  $\rho(r) \propto r^{-1}$ . We estimated the radius of a GMC with  $R = \sqrt{S/\pi}$ , where  $S$  is the cloud area within 30% levels of the  $^{12}\text{CO}$  peak integrated intensity. The velocity dispersion is adopted as the averaged value of each pixel in a GMC. Then, the  $X_{\text{CO}}$  factor using virial methods is expressed as

$$X_{\text{CO,vir}} = \frac{M_{\text{vir}}}{\mu_{\text{H}_2} m_{\text{H}} L_{\text{CO}}} [\text{cm}^{-2} (\text{K km s}^{-1})^{-1}], \quad (15)$$

where  $\mu_{\text{H}_2} \sim 2.8$  is the mean molecular weight per hydrogen molecule (Appendix A.1 in Kauffmann et al. 2008),  $m_{\text{H}} = 1.67 \times 10^{-24} \text{ g}$  is proton mass and  $L_{\text{CO}}$  is the  $^{12}\text{CO}$  total luminosity. Table 3 shows the results of the  $X_{\text{CO}}$  factor in each GMC obtained by the virial methods. The ratio of averaged  $X_{\text{CO}}$  taken from the virial mass and CO isotopologues is  $1.80 \pm 0.52$ .

## 6 SUMMARY

The conclusions of this paper are summarized as follows:

- (i) We studied the correlation between  $^{12}\text{CO}$  and  $^{13}\text{CO}$  intensities toward the Galactic GMCs W51A, W33, N35-N36 complex, W49A, M17SW, G12.02-00.03, W43, and M16 using the FUGIN CO survey data taken with the Nobeyama 45 m telescope.
- (ii) All the GMCs show intensity saturation of the  $^{12}\text{CO}$  line in regions with high brightness of  $^{13}\text{CO}$ .
- (iii) We also present high-resolution  $X_{\text{CO,iso}}$  maps made from the correlations of the CO isotopologues, which revealed local variability

**Table 3.** Physical parameters and  $X_{\text{CO, vir}}$  using virial method

Name	$R$ [pc]	$\sigma_v$ [km s <sup>-1</sup> ]	$M_{\text{vir}}$ [ $M_{\odot}$ ]	$L_{\text{CO}}$ [K km s <sup>-1</sup> pc <sup>2</sup> ]	$X_{\text{CO, vir}}$ [ $\times 10^{20}$ cm <sup>-2</sup> (K km s <sup>-1</sup> ) <sup>-1</sup> ]	$X_{\text{CO, iso}}/X_{\text{CO, vir}}$
(1)	(2)	(3)	(4)	(5)	(6)	(7)
W51A	6.3	4.2	$1.2 \times 10^5$	$3.5 \times 10^4$	1.51	1.5
W33	6.5	2.5	$4.3 \times 10^4$	$1.7 \times 10^4$	1.15	1.8
N35-N36	32	4.4	$6.2 \times 10^5$	$3.8 \times 10^5$	0.73	3.0
W49A	4.8	4.8	$1.2 \times 10^5$	$2.3 \times 10^4$	2.21	1.2
M17 SW	2.6	3.0	$2.4 \times 10^4$	$6.1 \times 10^3$	1.74	1.2
G012.02-00.03	7.1	2.4	$4.2 \times 10^4$	$7.7 \times 10^3$	2.47	0.68
W43	20	4.0	$3.2 \times 10^5$	$2.5 \times 10^5$	0.58	3.8
M16	6.0	2.1	$2.9 \times 10^4$	$1.3 \times 10^4$	1.01	2.1
Average	11	3.4	$1.7 \times 10^5$	$9.2 \times 10^4$	$1.43 \pm 0.68$	$1.80 \pm 0.52^*$

Columns: (1) GMC names (2) Cloud radius defined by the %30 levels of the peak integrated intensity (3) Mean velocity dispersion in a molecular cloud (4) Virial mass (5)  $^{12}\text{CO}$  luminosity (6) The  $X_{\text{CO}}$  factor derived by the virial mass. (7) Ratio of  $X_{\text{CO, iso}}$  to  $X_{\text{CO, vir}}$ . \*The averaged value is calculated from the ratio of averaged  $X_{\text{CO, iso}}$  and  $X_{\text{CO, vir}}$ .

of  $X_{\text{CO, iso}}$  in each GMC. We also show that the  $X_{\text{CO, iso}}$  monotonically decreases with increasing  $^{12}\text{CO}$  brightness temperature.

(iv) The averaged value of all GMCs is calculated to be  $X_{\text{CO, iso}} = (2.17 \pm 0.27) \times 10^{20}$  cm<sup>-2</sup> (K km s<sup>-1</sup>)<sup>-1</sup>, which is consistent within the margin of error with the reported values in the previous review.

(v) We show that  $X_{\text{CO, iso}}$  increases with the Galactocentric distance in accordance with the previous works while suggesting a larger value for the Galactic Centre by a factor of 3 compared to that by [Arimoto et al. \(1996\)](#).

(vi) The averaged value of the  $X_{\text{CO}}$  factor taken from the virial mass and CO isotopologues of GMCs is consistent within the error by a factor of 2.

## ACKNOWLEDGEMENTS

The authors are grateful to the anonymous referee for carefully reading our manuscript and giving us thoughtful suggestions, which greatly improved this paper. We are grateful to Dr. Shinji Fujita of the University of Tokyo and Prof. Toshihiro Handa of Kagoshima University for useful comments on data analysis and discussion. The authors would like to thank the FUGIN project members for the CO data observed by the Nobeyama 45-m telescope. The Nobeyama 45-m radio telescope is operated by the Nobeyama Radio Observatory. We utilized the Python software package for astronomy ([Astropy Collaboration et al. 2013](#)), NumPy ([van der Walt et al. 2011](#)), Matplotlib ([Hunter 2007](#)), IPython ([Perez, & Granger 2007](#)), CASA ([CASA Team et al. 2022](#)), and APLpy ([Robitaille & Bressert 2012](#)).

**Data availability:** The data underlying this article are available in <http://nro-fugin.github.io>. The FUGIN CO data were retrieved from the JVO portal <http://jvo.nao.ac.jp/portal> operated by ADC/NAOJ. The JCMT COHRS cube data is downloaded from the CANFAR data archive ([Gaudet et al. 2009](#)).

**Conflict of interest:** The authors declare that there is no conflict of interest.

## REFERENCES

Abdo, A. A., Ackermann, M., Ajello, M., et al. 2010, *ApJ*, 710, 133

Arimoto, N., Sofue, Y., & Tsujimoto, T. 1996, *PASJ*, 48, 275

Astropy Collaboration, Robitaille, T. P., Tollerud, E. J., et al. 2013, *A&A*, 558, A33

Blitz, L., Fukui, Y., Kawamura, A., et al. 2007, *Protostars and Planets V*, 81. doi:10.48550/arXiv.astro-ph/0602600

Bloemen, J. B. G. M., Strong, A. W., Mayer-Hasselwander, H. A., et al. 1986, *A&A*, 154, 25

Bolatto, A. D., Wolfire, M., & Leroy, A. K. 2013, *ARA&A*, 51, 207

CASA Team, Bean, B., Bhatnagar, S., et al. 2022, *PASP*, 134, 114501. doi:10.1088/1538-3873/ac9642

Chevanne, M., Krumholz, M. R., McLeod, A. F., et al. 2023, *Astronomical Society of the Pacific Conference Series*, 534, 1. doi:10.48550/arXiv.2203.09570

Dame, T. M., Hartmann, D., & Thaddeus, P. 2001, *ApJ*, 547, 792. doi:10.1086/318388

Dempsey, J. T., Thomas, H. S., & Currie, M. J. 2013, *ApJS*, 209, 8. doi:10.1088/0067-0049/209/1/8

Dickman, R. L. 1978, *ApJS*, 37, 407

Dobbs, C. L., Krumholz, M. R., Ballesteros-Paredes, J., et al. 2014, *Protostars and Planets VI*, 3. doi:10.2458/azu\_uapress\_9780816531240-ch001

Enokiyama, R., Torii, K., Schultheis, M., et al. 2014, *ApJ*, 780, 72. doi:10.1088/0004-637X/780/1/72

Frerking, M. A., Langer, W. D., & Wilson, R. W. 1982, *ApJ*, 262, 590

Fukui, Y., Okamoto, R., Kaji, R., et al. 2014, *ApJ*, 796, 59. doi:10.1088/0004-637X/796/1/59

Fukui, Y. & Kawamura, A. 2010, *ARA&A*, 48, 547. doi:10.1146/annurev-astro-081309-130854

Fujita, S., Torii, K., Kuno, N., et al. 2021, *PASJ*, 73, S172. doi:10.1093/pasj/psz028

Fujita, S., Ito, A. M., Miyamoto, Y., et al. 2023, *PASJ*, 75, 279. doi:10.1093/pasj/psac104

Gaudet, S., Dowler, P., Goliath, S., et al. 2009, *Astronomical Data Analysis Software and Systems XVIII*, 411, 185

Genzel, R., Tacconi, L. J., Combes, F., et al. 2012, *ApJ*, 746, 69. doi:10.1088/0004-637X/746/1/69

Goldreich, P., & Kwan, J. 1974, *ApJ*, 189, 441

Hayashi, K., Okamoto, R., Yamamoto, H., et al. 2019, *ApJ*, 878, 131

Hayashi, K., Mizuno, T., Fukui, Y., et al. 2019, *ApJ*, 884, 130

Heyer, M. & Dame, T. M. 2015, *ARA&A*, 53, 583. doi:10.1146/annurev-astro-082214-122324

Hunter, J. D. 2007, *Computing in Science and Engineering*, 9, 90

Israel, F. P. 1997, *A&A*, 328, 471. doi:10.48550/arXiv.astro-ph/9709194

Kamazaki, T., Okumura, S. K., Chikada, Y., et al. 2012, *PASJ*, 64, 29. doi:10.1093/pasj/64.2.29

Kauffmann, J., Bertoldi, F., Bourke, T. L., et al. 2008, *A&A*, 487, 993.

- doi:10.1051/0004-6361:200809481
- Kohno, M., Torii, K., Tachihara, K., et al. 2018, PASJ, 70, S50. doi:10.1093/pasj/psx137
- Kohno, M., Tachihara, K., Torii, K., et al. 2021, PASJ, 73, S129. doi:10.1093/pasj/psaa015
- Kuno, N., et al. 2011, in Proc. 2011 XXXth URSI General Assembly and Scientific Symposium (New York: IEEE), 3670<sup>1</sup>
- Langer, W. D., Wilson, R. W., Goldsmith, P. F., et al. 1989, ApJ, 337, 355. doi:10.1086/167108
- Lee, M.-Y., Stanimirović, S., Wolfire, M. G., et al. 2014, ApJ, 784, 80. doi:10.1088/0004-637X/784/1/80
- Lee, C., Leroy, A. K., Bolatto, A. D., et al. 2018, MNRAS, 474, 4672. doi:10.1093/mnras/stx2760
- Leroy, A. K., Bolatto, A., Gordon, K., et al. 2011, ApJ, 737, 12
- Lin, S.-J., Shimajiri, Y., Hara, C., et al. 2016, ApJ, 826, 193. doi:10.3847/0004-637X/826/2/193
- Liszt, H. S., Pety, J., & Lucas, R. 2010, A&A, 518, A45. doi:10.1051/0004-6361/201014510
- Lombardi, M., Alves, J., & Lada, C. J. 2006, A&A, 454, 781. doi:10.1051/0004-6361:20042474
- Minamidani, T., Nishimura, A., Miyamoto, Y., et al. 2016, Proc. SPIE, 99141Z
- Miyawaki, R., Hayashi, M., & Hasegawa, T. 2022, PASJ, 74, 128. doi:10.1093/pasj/psab113
- Mizuno, N., Rubio, M., Mizuno, A., et al. 2001, PASJ, 53, L45. doi:10.1093/pasj/53.6.L45
- Muraoka, K., Homma, A., Onishi, T., et al. 2017, ApJ, 844, 98. doi:10.3847/1538-4357/aa7a0b
- Murase, T., Handa, T., Hirata, Y., et al. 2022, MNRAS, 510, 1106. doi:10.1093/mnras/stab3472
- Nakajima, T., Inoue, H., Fujii, Y., et al. 2019, PASJ, 71, S17. doi:10.1093/pasj/psy112
- Nishimura, A., Minamidani, T., Umemoto, T., et al. 2018, PASJ, 70, S42. doi:10.1093/pasj/psx149
- Nishimura, A., Fujita, S., Kohno, M., et al. 2021, PASJ, 73, S285. doi:10.1093/pasj/psaa083
- Ohno, T., Tokuda, K., Konishi, A., et al. 2023, ApJ, 949, 63. doi:10.3847/1538-4357/accadb
- Oka, T., Hasegawa, T., Sato, F., et al. 1998, ApJS, 118, 455. doi:10.1086/313138
- Okamoto, R., Yamamoto, H., Tachihara, K., et al. 2017, ApJ, 838, 132
- Park, G., Currie, M. J., Thomas, H. S., et al. 2023, ApJS, 264, 16. doi:10.3847/1538-4365/ac9b59
- Perez, F., & Granger, B. E. 2007, Computing in Science and Engineering, 9, 21
- Pitts, R. L. & Barnes, P. J. 2021, ApJS, 256, 3. doi:10.3847/1538-4365/ac063d
- Planck Collaboration, Ade, P. A. R., Aghanim, N., et al. 2011, A&A, 536, A19. doi:10.1051/0004-6361/201116479
- Planck Collaboration, Fermi Collaboration, Ade, P. A. R., et al. 2015, A&A, 582, A31
- Pineda, J. E., Caselli, P., & Goodman, A. A. 2008, ApJ, 679, 481
- Remy, Q., Grenier, I. A., Marshall, D. J., et al. 2017, A&A, 601, A78
- Reid, M. J., Menten, K. M., Brunthaler, A., et al. 2019, ApJ, 885, 131. doi:10.3847/1538-4357/ab4a11
- Robitaille, T., & Bressert, E. 2012, APLpy: Astronomical Plotting Library in Python, ascl:1208.017
- Rosolowsky, E., Engargiola, G., Plambeck, R., et al. 2003, ApJ, 599, 258. doi:10.1086/379166
- Sakamoto, S. 1996, ApJ, 462, 215. doi:10.1086/177142
- Sandstrom, K. M., Leroy, A. K., Walter, F., et al. 2013, ApJ, 777, 5. doi:10.1088/0004-637X/777/1/5
- Sanna, A., Reid, M. J., Menten, K. M., et al. 2014, ApJ, 781, 108. doi:10.1088/0004-637X/781/2/108
- Sawada, T., Ikeda, N., Sunada, K., et al. 2008, PASJ, 60, 445. doi:10.1093/pasj/60.3.445
- Scoville, N. Z., Yun, M. S., Clemens, D. P., et al. 1987, ApJS, 63, 821. doi:10.1086/191185
- Sodroski, T. J., Odegard, N., Dwek, E., et al. 1995, ApJ, 452, 262. doi:10.1086/176297
- Sofue, Y., & Kataoka, J. 2016, PASJ, 68, L8
- Sofue, Y., Kohno, M., Torii, K., et al. 2019, PASJ, 71, S1
- Sofue, Y. 2019a, PASJ, 71, 104. doi:10.1093/pasj/psz090
- Sofue, Y. 2019b, PASJ, 71, 121. doi:10.1093/pasj/psz106
- Sofue, Y. 2020a, PASJ, 72, 21. doi:10.1093/pasj/psz143
- Sofue, Y. 2020b, MNRAS, 492, 5966
- Sofue, Y. & Kohno, M. 2020, MNRAS, 497, 1851. doi:10.1093/mnras/staa2056 (Paper I)
- Sofue, Y. 2021, Galaxies, 9, 13. doi:10.3390/galaxies9010013
- Sofue, Y. 2022, MNRAS, 509, 5809. doi:10.1093/mnras/stab3091
- Solomon, P. M., Rivolo, A. R., Barrett, J., et al. 1987, ApJ, 319, 730
- Strong, A. W., Bloemen, J. B. G. M., Dame, T. M., et al. 1988, A&A, 207, 1
- Tokuyama, S., Oka, T., Takekawa, S., et al. 2019, PASJ, 71, S19. doi:10.1093/pasj/psy150
- Torii, K., Kudo, N., Fujishita, M., et al. 2010, PASJ, 62, 1307. doi:10.1093/pasj/62.5.1307
- Torii, K., Fujita, S., Matsuo, M., et al. 2018, PASJ, 70, S51. doi:10.1093/pasj/psy019
- Torii, K., Fujita, S., Nishimura, A., et al. 2019, PASJ, 71, S2. doi:10.1093/pasj/psz033
- Umemoto, T., Minamidani, T., Kuno, N., et al. 2017, PASJ, 69, 78
- van der Walt, S., Colbert, S. C., & Varoquaux, G. 2011, Computing in Science and Engineering, 13, 22
- VERA Collaboration, Hirota, T., Nagayama, T., et al. 2020, PASJ, 72, 50. doi:10.1093/pasj/psaa018
- Weiß, A., Neininger, N., Hüttemeister, S., et al. 2001, A&A, 365, 571. doi:10.1051/0004-6361:20000145
- Wilson, C. D. 1995, ApJ, 448, L97. doi:10.1086/309615
- Wilson, T. L., Rohlf, K., & Hüttemeister, S. 2009, Tools of Radio Astronomy, by Thomas L. Wilson; Kristen Rohlf and Susanne Hüttemeister. ISBN 978-3-540-85121-9. Published by Springer-Verlag, Berlin, Germany, 2009. doi:10.1007/978-3-540-85122-6
- Yamagishi, M., Kaneda, H., Ishihara, D., et al. 2016, ApJ, 833, 163. doi:10.3847/1538-4357/833/2/163
- Yasuda, A., Kuno, N., Sorai, K., et al. 2023, PASJ, 75, 743. doi:10.1093/pasj/psad034
- Yoda, T., Handa, T., Kohno, K., et al. 2010, PASJ, 62, 1277. doi:10.1093/pasj/62.5.1277

## APPENDIX A: EFFECT OF THE PHYSICAL RESOLUTION

To confirm that the scatter plots shown in Figure 2 do not depend on the physical resolutions due to different distances to the GMCs, we smoothed the data and made the same physical resolution maps of  $\sim 1$  pc (Figure A1). The result is shown in Figure A2, which is almost identical to the original plots. We thus confirm that the results are not affected by the different distances of the objects.

<sup>1</sup> <http://ieeexplore.ieee.org/xpl/articleDetails.jsp?arnumber=6051296>



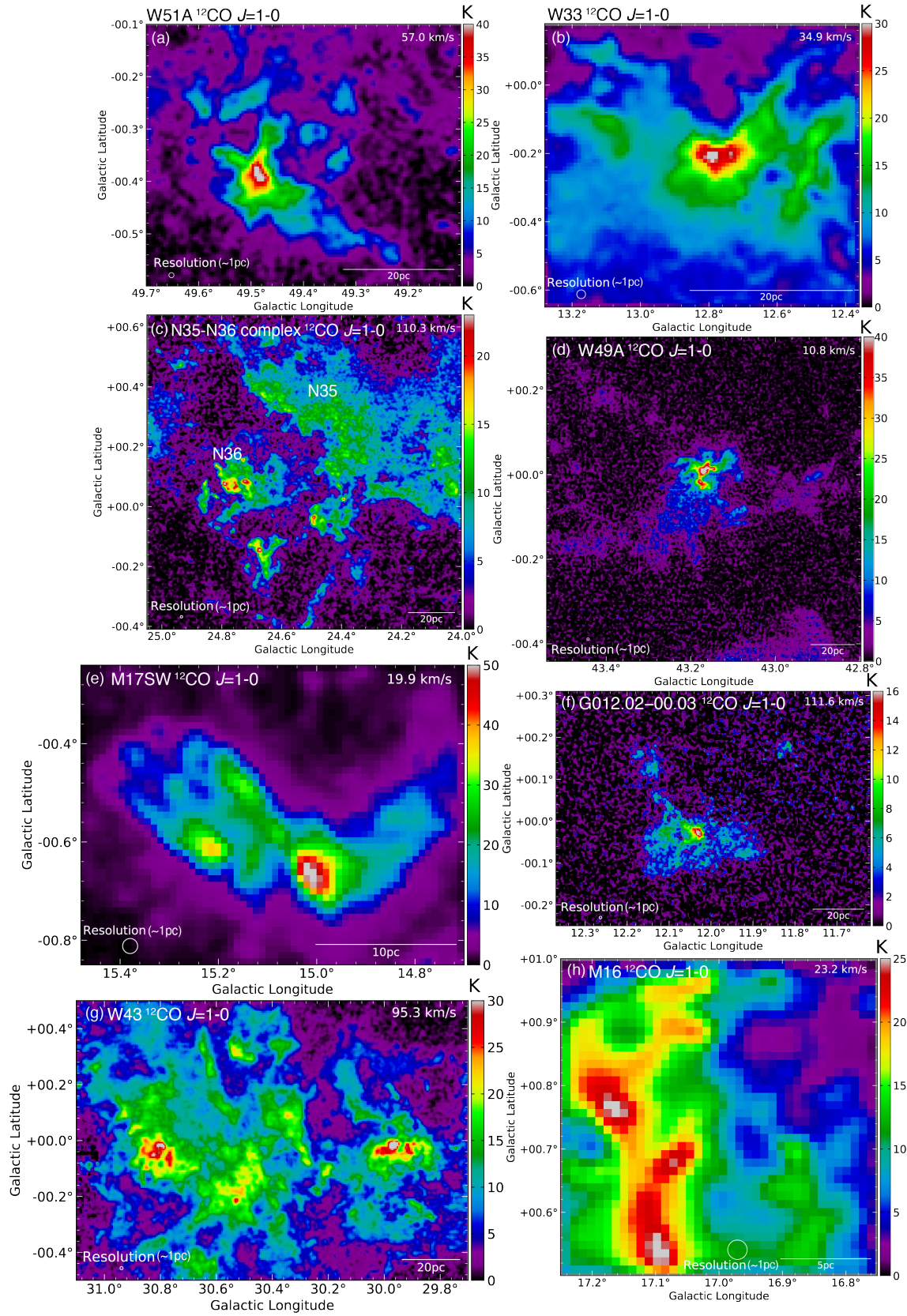


Figure A1. Same as Figure 1, but the data was smoothed to the same physical resolution of  $\sim 1$  pc.

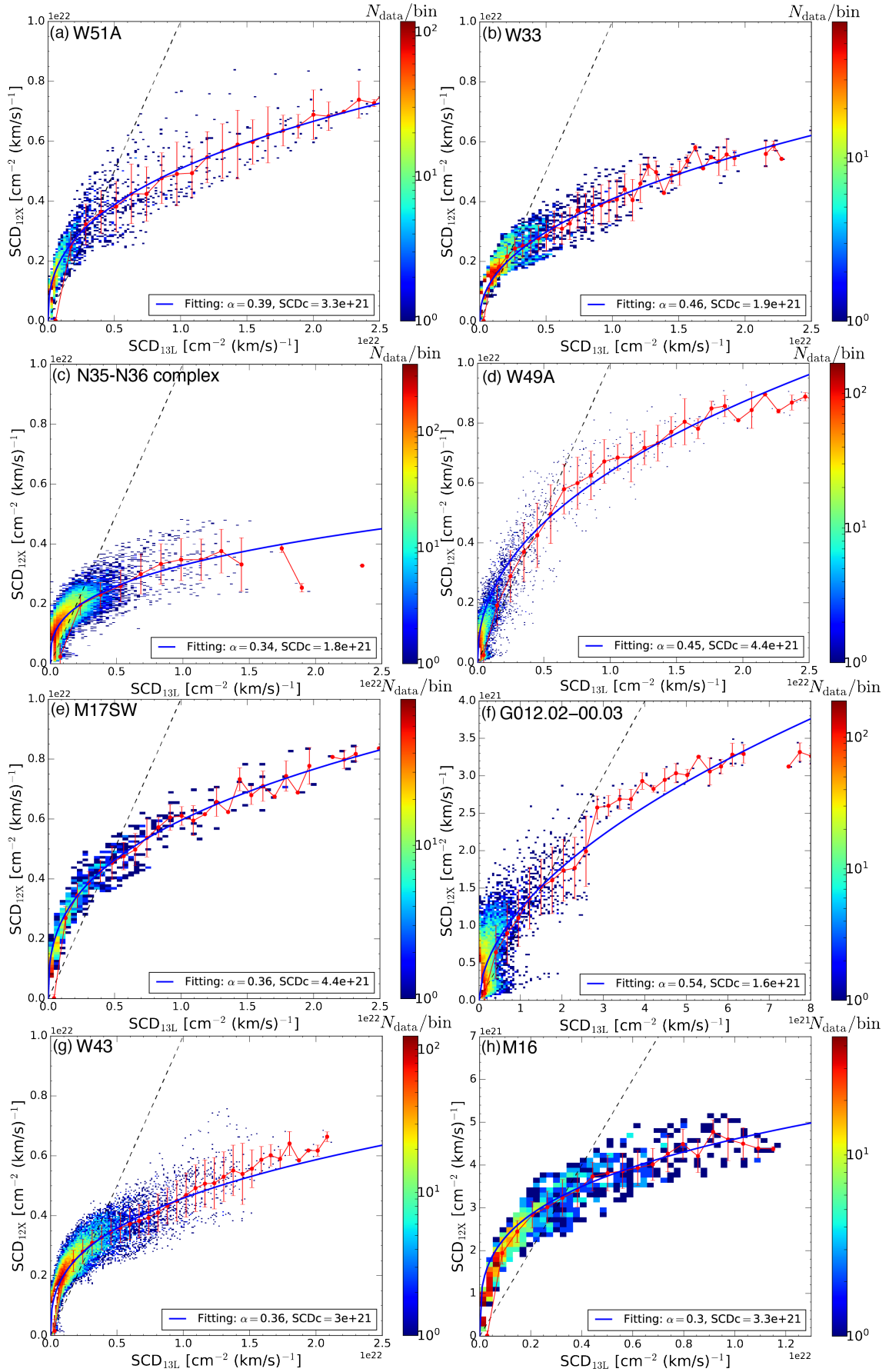


Figure A2. Same as Figure 2, but the data was smoothed to the same physical resolution of  $\sim 1$  pc.